

Explainable autoencoder for neutron star dense matter parameter estimation

Francesco Di Clemente

INFN Sezione di Ferrara, Via Saragat 1, 44122 Ferrara, Italy

E-mail: fdiclemente@fe.infn.it

Matteo Scialpi

Dipartimento di Fisica e Scienze della Terra, Università di Ferrara, Via Saragat 1, 44122 Ferrara, Italy

INFN Sezione di Ferrara, Via Saragat 1, 44122 Ferrara, Italy

E-mail: matteo.scialpi@unife.it

Michał Bejger

INFN Sezione di Ferrara, Via Saragat 1, 44122 Ferrara, Italy

Nicolaus Copernicus Astronomical Center, Polish Academy of Sciences, Bartycka 18, 00-716 Warszawa, Poland

E-mail: bejger@fe.infn.it

Abstract. We present a physics-informed autoencoder designed to encode the equation of state of neutron stars into an interpretable latent space. In particular the input will be encoded in the mass, radius, and tidal deformability values of a neutron star. Unlike traditional black-box models, our approach incorporates additional loss functions to enforce explainability in the encoded representations. This method enhances the transparency of machine learning models in physics, providing a robust proof-of-concept tool to study compact stars data. Our results demonstrate that the proposed autoencoder not only accurately estimates the EoS parameters and central density/pressure but also offers insights into the physical connection between equation of state and observable physical quantities. This framework conceptualizes the physical differential equations themselves as the “encoders”, allowing interpretability of the latent space.

1. Introduction

Autoencoders (AEs), first introduced in [1] (see [2–4] for review) belong to a class of artificial neural networks (NNs) designed for unsupervised learning tasks. Their primary function is to encode input data into a lower-dimensional latent space and subsequently decode it to reconstruct the original input. Therefore, an AE typically consists of two main components: the encoder, which compresses the input data into a compact representation, and the decoder, which reconstructs the input data from this

representation. The primary advantage of AEs is their ability to learn efficiently without supervision, making them useful for dimensionality reduction, anomaly detection, and data denoising, see [5, 6].

Despite their effectiveness, AEs still function as “black boxes”, providing limited insight into the internal workings of the model and the learned latent representations. This lack of transparency has been frequently criticized, especially in scientific fields where interpretability is essential for validating the results of machine learning (ML) models [7, 8]. EXplainable Artificial Intelligence (XAI) seeks to address this issue by developing models and methods that elucidate the decision-making process for humans [9].

In physics, the necessity for explainable models is especially critical. This paper is focused specifically on the astrophysics of neutron stars (NSs), where the relationship between the microphysical properties of dense matter - the equation of state (EoS) parameters, such as the relation between pressure and density, and their values at the center of the NS - and NS macroscopical observable properties such as the mass, radius, and tidal deformability can be determined by integrating the Tolman-Oppenheimer-Volkoff (TOV) equations of stellar hydrostatic equilibrium [10, 11], and analogous equation for quadrupole static tidal deformability, see e.g. [12, 13]. The EoS is here an input to the TOV equations, whereas macroscopic NS parameters are the output. Given observations of functionals of the EoS, e.g. masses and radii, the inverse TOV relation is not straightforward because, in principle, a NS with the same mass and radius can correspond to multiple EoSs and/or central density values. ML analysis may aid in constraining the EoS based on physical observations, as ML solutions, including AEs, offer a powerful alternative for approximating these relationships [14, 15]. In the past, several approaches explored the application of NNs as inference tools for NS properties and nuclear matter properties from the observations [16–30]. Nevertheless, ensuring that these models provide interpretable and physically meaningful results remains a challenge.

We propose here a physics-informed version of an AE architecture, PIA (Physics-Informed Autoencoder), specifically designed to not only reproduce the parameters of the EoS for a given set of NS observations, but also to encode them into physically interpretable quantities in the AE’s latent space, effectively making it interpretable. This approach goes beyond conventional AEs by incorporating additional loss functions that guide the encoding process towards representations that are closely aligned with the underlying physical principles. In particular, the encoding in the latent space is enforced to reflect solutions to the TOV equations that govern the system, treating these solutions as encoded versions of the physical parameters and boundary conditions. The TOV equations serve here as the true encoders, mapping the physical parameters into latent space representations. The model in turn acts as an approximation to this process, learning to replicate the encoding process that would otherwise be performed by solving the TOV equations directly. This hybrid approach effectively transforms the AE into a physically-informed neural network (PINN), where the latent space is no

longer an abstract feature space but instead a space capable of incorporating one or more physical laws. Unlike traditional PINNs, where physics is incorporated at the level of solving partial differential equations (PDEs) [31–33], in PIA the physics is incorporated as algebraic constraints. These constraints guide the network by enforcing relationships that are consistent with known physical laws, ensuring that the network adheres to them while training.

In the following, in Sect. 2 we describe the dataset, present the AE methodology and our implementation choices in Sect. 3, whereas Sect. 4 contains the results of our implementation and experiments. Section 5 discusses the implications and potential applications of our findings.

2. Dataset

The dataset is composed of pairs of data: a parameterized EoS, which for the sake of this work’s proof-of-concept presentation is meant to approximate a microphysical description of dense-matter properties, and solutions of the TOV equations of hydrostatic equilibria of NSs, i.e. functionals of EoS in the form of global NS quantities: masses, radii and tidal deformabilities. These integrated quantities for a given NS relate to a given EoS, and are ”labeled” by EoS parameters in the center of the NS (e.g. the central density). Therefore, for a given EoS, one can obtain a sequence of mass-radius-tidal deformability by adopting different central parameters along the EoS (see Fig. 1).

In this study, we approximate the EoS for NS matter using a piecewise polytropic model representation, where the pressure p is related to the density ρ through the relation:

$$p(\rho) = K\rho^\gamma, \tag{1}$$

with K a proportionality constant, and γ the polytropic index. The energy density $\epsilon(\rho)$ as a function of mass density ρ is derived from the thermodynamic relationship between pressure and energy density and taking into account the rest mass density zero limit (at which $\epsilon = \rho$) it is expressed as:

$$\epsilon(\rho) = \rho + \frac{1}{\gamma_i - 1}p(\rho). \tag{2}$$

While the simple polytropic form captures the general behavior of matter at specific density ranges, it is insufficient to describe the full range of densities found in NSs, particularly as nuclear matter undergoes significant changes in behavior at different densities.

To address this limitation, the piecewise polytropic approach divides the density range into multiple regions, each governed by its own K and γ parameters. Following [35], we define three density regions within our model, and hence three parameters γ_1 ,

Explainable autoencoder for neutron star dense matter parameter estimation

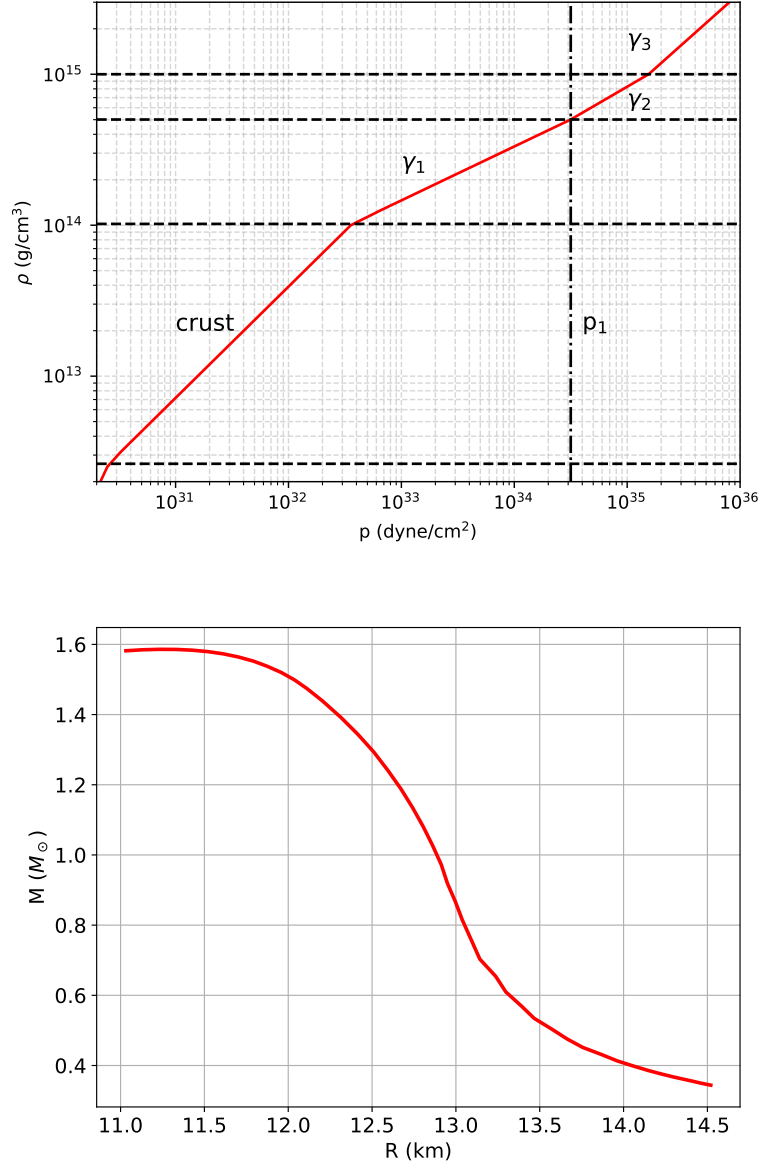


Figure 1. Top panel: Example of a piecewise-polytropic EoS, described in Eq. 3, with $p_1 = 10^{34.5}$, $\gamma_1 = 2.8$, $\gamma_2 = 2.3$ and $\gamma_3 = 1.5$. Bottom panel: $M(R)$ diagram of the EoS. Note that neither the EoS nor the $M(R)$ diagram is representative of current observational constraints for NSs, specifically the constraints on the maximum mass, $\simeq 2 M_\odot$ [34]. The values of γ_i have been chosen solely to visualize the piecewise segmentation of the EoS.

γ_2 and γ_3 :

$$p(\rho) = \begin{cases} K_1 \rho^{\gamma_1}, & \text{if } \rho \leq \rho_1, \\ K_2 \rho^{\gamma_2}, & \text{if } \rho_1 < \rho \leq \rho_2, \\ K_3 \rho^{\gamma_3}, & \text{if } \rho > \rho_2, \end{cases} \quad (3)$$

where ρ_1 and ρ_2 are the density thresholds dividing the regions, and continuity conditions ensure that the pressure is consistent at the boundaries. The constants K_2 and K_3 are computed based on the continuity requirements at $\rho_1 = 10^{14.7} \text{ g/cm}^3$ and $\rho_2 = 10^{15} \text{ g/cm}^3$, such that

$$K_1 = \rho_1^{-\gamma_1}, \quad (4)$$

$$K_2 = K_1 \rho_1^{\gamma_1 - \gamma_2}, \quad (5)$$

$$K_3 = K_2 \rho_2^{\gamma_2 - \gamma_3}, \quad (6)$$

with K_1 directly related to the pressure p_1 and density ρ_1 , ensuring the proper initialization of the first polytropic segment.

The choice of ρ_1 and ρ_2 is based on typical densities found within NSs, particularly in regions critical for studying dense matter, and is not significantly reducing the generality of the EoS model. We assume that the low-density part of the EoS (the ‘‘crust’’), attached at ρ_0 is well-approximated by the SLy4 EoS [36]. By requirements of mechanical and chemical equilibrium, the relevant free parameters in our EoS model are finally p_1 (the pressure between the segment 1 and the segment 2), γ_1 , γ_2 and γ_3 and ρ_0 .

In order to build our dataset, we solve the TOV equations and the tidal deformability equation using an implementation from [37] for a set of EoSs with parameters varying within fixed ranges \ddagger . To achieve this, we employ a systematic approach in which the parameters of the piecewise polytropic EoS, such as the polytropic indices γ_i are varied within intervals that are chosen to produce physical quantities consistent with theoretical and observational constraints [38]. This method ensures coverage of a wide range of possible NS configurations.

3. Model loss functions and PIA architecture

Here we employ a customized version of an AE. AEs learn to encode input data into a usually lower-dimensional latent space and then decode it back to the original input. Mathematically, an AE consists of two main parts: the encoder function f_θ and the decoder function g_ϕ , where θ and ϕ are the parameters of the encoder and decoder, respectively.

\ddagger The dataset has been made by sampling from uniform distributions of $\gamma_i \in [1.3, 4]$ and $\log_{10}(p_1) \in [34.001, 34.900]$.

3.1. Encoder and Decoder Functions

Given an input $\mathbf{x} \in \mathbb{R}^n$, the encoder maps this input to a latent representation $\mathbf{z} \in \mathbb{R}^m$, where usually $m < n$:

$$\mathbf{z} = f_{\theta}(\mathbf{x}). \quad (7)$$

Here, f_{θ} represents the encoder function parameterized by θ . The latent representation \mathbf{z} aims at capturing the essential features of the input data in, usually, a lower-dimensional space. The decoder maps the latent representation back to the reconstructed input $\hat{\mathbf{x}}$:

$$\hat{\mathbf{x}} = g_{\phi}(\mathbf{z}). \quad (8)$$

In this expression, g_{ϕ} denotes the decoder function parameterized by ϕ . The goal of the AE is to minimize the difference between the input \mathbf{x} and the output (reconstructed input) $\hat{\mathbf{x}}$. This is typically achieved using a loss function, such as the Mean Squared Error (MSE):

$$\mathcal{L}_{\text{MSE}} = \|\mathbf{x} - \hat{\mathbf{x}}\|^2 = \|\mathbf{x} - g_{\phi}(f_{\theta}(\mathbf{x}))\|^2. \quad (9)$$

A key limitation of the standard AE architecture lies in the fact that the latent representation is not directly involved in the training process, there is typically no specific term in the loss function that governs the structure or meaning of the latent space. This design is intentional, as AEs are primarily focused on data reconstruction, with the latent space serving as an abstract intermediate. However, this abstraction results in a lack of interpretability, as the latent variables do not necessarily correspond to physically meaningful quantities.

We recognize that, in the traditional setup, the latent space is not intended to be explainable. However, by introducing targeted constraints that encode known physical relationships, such as those derived from the EoS, we can guide the AE toward a more interpretable latent space. In doing so, we move closer to an explainable architecture where the latent variables have clear physical interpretations. This allows the model not only to reconstruct data accurately but also to offer insights into the underlying physics, thereby addressing one of the key challenges in using machine learning for scientific discovery.

3.2. Physics-Informed Loss Function

Our goal is to ensure that the trained latent representations are physically interpretable, therefore we introduce an additional loss term that enforces consistency with the physical equations governing the system. Specifically, we incorporate a physics-informed loss that penalizes deviations from the expected behavior dictated by the solutions of the TOV equation in the latent space, in order to “force” the encoding in a explainable space. In addition we add two physics-informed loss term based on compactness and tidal deformability. These loss terms play a crucial role in guiding the network toward the global minimum of the total loss function. By embedding these physical constraints directly into the loss, we effectively enforce that the global minimum corresponds to

regions where the underlying physical conditions hold true, see the Appendix A for details.

Note that in the following, we use the t subscript on variables to denote their ground truth values, where t stands for “target”, representing the values we aim to reproduce. Conversely, variables with a hat (e.g., \hat{x}) will always refer to the corresponding reconstructed values produced by the network.

The physics-informed terms act as a form of regularization, steering the optimization process toward solutions that are not only mathematically optimal, but also physically meaningful. This approach ensures that the network prioritizes configurations consistent with established physical relationships, thereby enhancing the interpretability and reliability of the model’s outputs. We will list below the terms making up the total loss \mathcal{L} , combining the reconstruction loss \mathcal{L}_{MSE} , the physics-informed loss terms $\mathcal{L}_{\text{physics}}$, as well as the boundary loss \mathcal{L}_{b} :

$$\mathcal{L} = \mathcal{L}_{\text{MSE}} + \mathcal{L}_{\text{physics}} + \mathcal{L}_{\text{b}}. \quad (10)$$

This allows flexibility in balancing the model’s fidelity to the input data against its adherence to physically meaningful relationships in the latent space. The combined loss function enforces both accurate data reconstruction and the interpretability of the latent space through physically motivated constraints. By integrating these terms, the model not only reconstructs the input data effectively but also encodes representations that align with known physical properties. Such alignment enhances the model’s interpretability, as it can then leverage the encoder and decoder parts of the network to test and explore physical data in a meaningful way. The parts of Eq. 10 are as follows.

Reconstruction Loss \mathcal{L}_{MSE} . The first term in the loss function \mathcal{L} is the standard MSE used in AEs, as described in subsection 3.1, which measures the difference between the actual parameters of the EoS— $\mathbf{p}_1, \gamma_1, \gamma_2, \gamma_3, \rho_0$ —and their reconstructed counterparts, denoted with a hat (e.g., $\hat{\mathbf{p}}_1, \hat{\gamma}_1$). This term ensures that the autoencoder learns to accurately reconstruct the input EoS parameters and the central density:

$$\mathcal{L}_{\text{MSE}} = \|(\hat{\mathbf{p}}_1, \hat{\gamma}_1, \hat{\gamma}_2, \hat{\gamma}_3, \hat{\rho}_0) - (\mathbf{p}_1, \gamma_1, \gamma_2, \gamma_3, \rho_0)_t\|^2. \quad (11)$$

Physics-Informed Latent Loss $\mathcal{L}_{\text{physics}}$. This loss term enforces specific physical relationships within the latent space, consisting of three contributions:

1. \mathcal{L}_{TOV} : It is the MSE between the encoded latent representations of mass \hat{M} , radius \hat{R} , and tidal deformability $\hat{\Lambda}$, and their corresponding target values M_t, R_t , and Λ_t . It ensures that the latent variables accurately reflect the physical properties as predicted by the TOV equations and the tidal deformability differential equation:

$$\mathcal{L}_{\text{TOV}} = \left\| (\hat{M}, \hat{R}, \hat{\Lambda}, \hat{C}) - (M, R, \Lambda, C)_t \right\|^2. \quad (12)$$

Although this is not strictly a physics-informed term, as it does not enforce any explicit physical relationships, it is essential for encoding the EoS into macroscopic variables.

Explainable autoencoder for neutron star dense matter parameter estimation

2. \mathcal{L}_C : This term is the MSE between the reconstructed compactness, $\hat{C} = \frac{\hat{M}}{\hat{R}}$, and the compactness value from the dataset, C_t . It preserves the correct mass-to-radius ratio, ensuring that the encoded representations maintain a physically meaningful compactness:

$$\mathcal{L}_C = \left\| \frac{\hat{M}}{\hat{R}} - C_t \right\|^2. \quad (13)$$

3. $\mathcal{L}_{\Lambda C}$: This term is the MSE between the predicted tidal deformability, $\hat{\Lambda}$, and an empirical estimate based on compactness, $f(\hat{C})$, sometimes called a “universal relation”. While not a strictly physical relationship, an empirical relationship exists between tidal deformability and compactness, which can act as an additional physical constraint within the loss function. By enforcing $\hat{\Lambda}$ to align with $f(\hat{C})$, the latent space reflects known correlations observed in compact stars physics:

$$\mathcal{L}_{\Lambda C} = \left\| \hat{\Lambda} - f\left(\frac{\hat{M}}{\hat{R}}\right) \right\|^2. \quad (14)$$

In this context, $f(C)$ is the inverse of a compactness-tidal deformability “universal relation”, expressed as:

$$C = \sum_i b_i (\log(\Lambda))^i, \quad (15)$$

where b_i are numerical coefficients provided in [39]. These empirical coefficients establish a polynomial relation between the compactness C and the logarithm of the tidal deformability Λ . Combining these three terms, the overall physics-informed loss is defined as follows:

$$\mathcal{L}_{\text{physics}} = \alpha \mathcal{L}_{\text{TOV}} + \beta \mathcal{L}_C + \delta \mathcal{L}_{\Lambda C}, \quad (16)$$

with weighting factors α , β and δ controlling the influence of the physical constraints relative to other terms. The inclusion of $\mathcal{L}_{\Lambda C}$ allows the model to leverage known empirical relationships, effectively guiding the AE towards a latent space that respects the established behavior of NS properties.

We are aware that the universal relation between tidal deformability and compactness (Eq. 15) may not hold in cases where strong first-order phase transitions occur within the NS [40], or in the case of strange stars, which exhibit an energy density discontinuity at the surface. Nevertheless, the use of this relation is justified within the context of our study for several reasons. First, the majority of NSs models adhere to EoS without such drastic phase transitions [38], meaning the universal relation provides a reasonable approximation for a wide range of astrophysical scenarios. Second, our model is designed as a proof-of-concept, where the primary aim is to explore the utility of embedding physical constraints within machine learning architectures.

It has to be noted that we utilize only algebraic physics-informed loss terms to guide the training of our NN. These loss terms can be broadly classified into two categories: *proper physical relations* and *empirical relations*.

Explainable autoencoder for neutron star dense matter parameter estimation

The proper physical relations are derived directly from first principles, such as conservation laws or fundamental equations governing the behavior of physical systems. These include, for example, even the simple constraint based on compactness \mathcal{L}_C , ensuring that the latent space and outputs adhere to well-established physical principles.

The empirical relations, on the other hand, are derived from observational or simulated data and represent approximate fits to known behavior. While these relationships may not come from exact physical derivations, they are needed to reinforce expected trends in the data. An example is the relationship between tidal deformability and compactness, which has been shown to hold for a broad range of NS models. Including such relations with the right weights helps to subtly enforce patterns that align with astrophysical observations or simulations, enhancing the physical interpretability of the NN. This dual approach ensures that the latent space and reconstructed parameters maintain both physical plausibility and consistency with observed behavior.

By including the tidal deformability–compactness relation of Eq. 15, we demonstrate how known empirical relationships can guide the learning process and improve the model’s ability to reflect physically meaningful properties within the latent space. This approach allows the model to capture the general behavior of NS matter, providing a foundation for further refinement should future work incorporate more complex EoS considerations.

Boundary loss \mathcal{L}_b . Last but not least, to ensure that the model’s predictions remain within physically realistic limits, we introduce a boundary loss term. This loss can be seen as an additional physics-informed constraint by explicitly informing the NN about the physical boundaries of the parameters. The boundary loss is designed to apply penalties only when the predictions violate these limits, using the ReLU activation function. Specifically, it penalizes outputs that fall below the minimum allowed values or exceed the maximum allowed values. The loss is calculated as

$$\mathcal{L}_b = \sum_i [\text{ReLU}^2(\gamma_{i,\text{mins}} - \gamma_{\text{output}}) + \text{ReLU}^2(\gamma_{\text{output}} - \gamma_{i,\text{maxs}})]. \quad (17)$$

Here, ReLU ensures that penalties are only applied when the outputs violate the feature-wise bounds. This mechanism improves the robustness and reliability of the outputs in modeling NS properties.

3.3. PIA structure

PIA structure is composed of the encoder and the decoder, each consisting of fully connected layers. The architecture is designed to progressively transform the input features into a latent representation and then reconstruct the data from this representation. While traditional AEs sequentially reduce the input dimensionality through progressively smaller intermediate layers, we propose an alternative approach where the latent space has a dimensionality comparable to the input. To effectively manage this network and establish a strong connection between the input and latent

space, the first layer after the input is significantly larger than the input itself, followed by subsequent layers that reduce the dimensionality back to the latent space, see Fig. 2 and Table 1 for the detailed structure.

This design choice is motivated by several considerations. The expanded layers that follow the input layer allow the NN to initially capture and process more complex features before compression. This can be particularly advantageous in scenarios where high-dimensional patterns exist in the data, as is the case in our study, which could be lost in early compression stages. The expanded layers act as a feature extraction mechanism, helping the model learn richer representations that mimic the behavior of differential equations and the construction of polytropic EoSs.

In certain tasks, such as those involving high-dimensional or highly structured data, e.g. cosmological data or physical simulations, the nature of the data may not lend itself well to immediate compression. By introducing layers with dimensions larger than the input size early in the NN, we allow the model to learn effectively the underlying relationships before enforcing a latent space bottleneck. While expanding the dimensionality of layers increases the capacity of the NN, the latent space, which serves as a physically informed constraint, ensures that the model does not simply memorize the input data. Instead, the model compresses the features into this constrained space, encouraging it to learn meaningful representations that capture the underlying physics. This latent space extraction helps preserve significant features in the data that relate to the physical processes being modeled. This architecture can be viewed as a hybrid approach, combining elements of traditional AEs to capture the physical features, by balancing expansion with subsequent compression.

As in traditional AEs, the decoder mirrors the structure of the encoder, expanding the latent space back to the original input dimensions. Starting from the four-dimensional latent vector, the decoder passes the data through four linear layers, with dimensionalities matching those of the encoder in reverse order.

Layer	Encoder	Decoder	Activation
Input	5	4 (latent)	SiLU
Hidden Layer 1	$5n$	$1n$	SiLU
Hidden Layer 2	$4n$	$2n$	SiLU
Hidden Layer 3	$3n$	$3n$	SiLU
Hidden Layer 4	$2n$	$4n$	SiLU
Output / Latent Space	4 (latent)	5	–
Dropout	Hidden Layers 1-3	Hidden Layers 1-3	$p = [0.1, 0.5]$

Table 1. NN structure: Layer dimensions for the encoder and decoder with n varied from 64 to 512 among the several experiments, see Sect. 4 for more details.

3.3.1. The Monte Carlo Dropout Experiments both in training and testing phase have been conducted using asymmetrical dropout values between the encoder and decoder. By applying smaller dropout values in the encoder compared to the decoder, we enforce

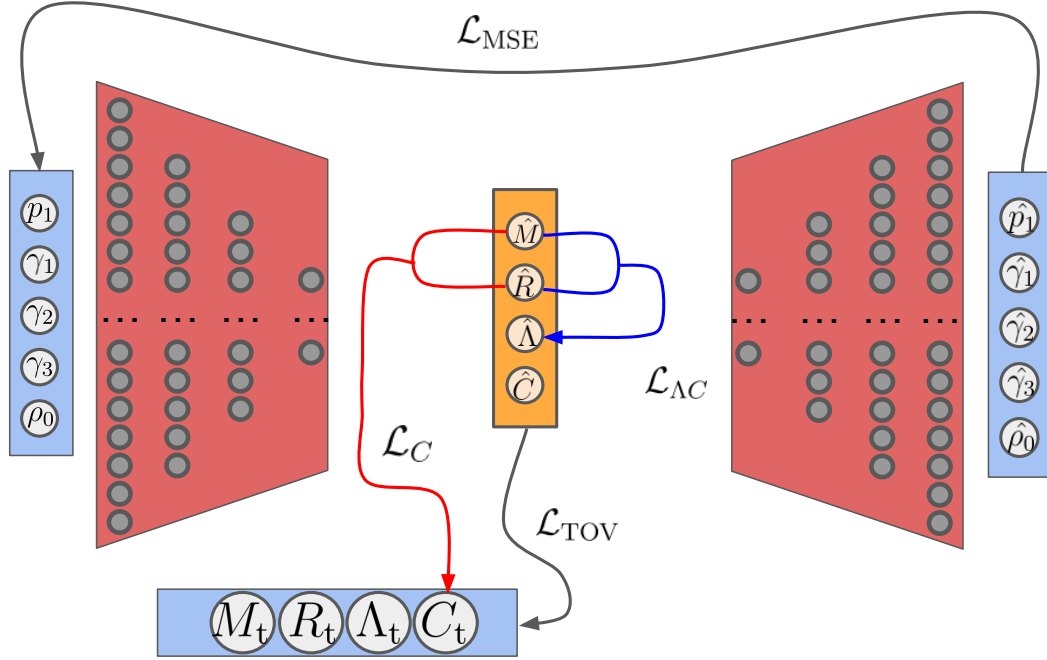


Figure 2. Schematic representation of the AE architecture with physics-informed loss terms. The input parameters $p_1, \gamma_1, \gamma_2, \gamma_3, \rho_0$ are passed through the encoder (left red block) to produce latent variables representing macroscopic quantities such as mass \hat{M} , radius \hat{R} , tidal deformability $\hat{\Lambda}$, and compactness \hat{C} in the latent space (orange block). The latent variables are constrained by physics-informed loss terms: \mathcal{L}_C (red arrow) for compactness, \mathcal{L}_{AC} (blue arrow) for the tidal deformability-compactness relation, and \mathcal{L}_{TOV} (gray arrow) enforcing consistency with the TOV equations. The decoder (right red block) reconstructs the EoS parameters $\hat{p}_1, \hat{\gamma}_1, \hat{\gamma}_2, \hat{\gamma}_3, \hat{\rho}_0$, with the reconstruction loss \mathcal{L}_{MSE} .

the fact that a specific combination of $(p_1, \gamma_1, \gamma_2, \gamma_3, \rho_0)$ leads to a unique combination of (M, R, Λ, C) . However, a given combination of (M, R, Λ, C) can correspond to several possible EoSs, which may differ based on the choice of the central density ρ_0 , a parameter that remains unobservable. This design reflects the physical reality that while macroscopic observables such as mass M , radius R , tidal deformability Λ , and compactness C are constrained by the underlying microphysics, the details of the EoS, introduce inherent degeneracies that cannot be directly disentangled from observational data alone. The asymmetrical dropout configuration serves to mirror this uncertainty by allowing the decoder to explore a broader range of possible EoS corresponding to the observed parameters, while the encoder remains more constrained, ensuring that the mapping from microphysical parameters to macroscopic observables is physically consistent.

During inference phase, dropout is applied in the decoder as the Monte Carlo

dropout, allowing for uncertainty estimation [41]. By repeatedly calling the decoder on the same input values, a distribution of reconstructed parameters for the EoS is generated. We chose not to apply the Monte Carlo dropout during the inference phase for M - R - Λ estimation. The primary reason for this decision is the absence of implicit degeneracy in the mapping from the EoS and central density to the NS observables.

Given a specific EoS and central density ρ_0 , these physical quantities are uniquely determined by solving the TOV equations. Unlike other scenarios where uncertainties or degeneracies in the input-output relationship necessitate uncertainty quantification, this deterministic nature eliminates the need for the Monte Carlo sampling. As a result, the predictions are precise and do not benefit from the distributional output that the Monte Carlo dropout would provide. This approach is well-suited for cases like studied here, where the physical system inherently lacks ambiguity in the relationship between the inputs and the informed latent space.

3.4. Training Process

The dataset, consisting of simulated NS parameters, was normalized to ensure that each feature was scaled to a predefined range, improving stability during training. The feature-wise minimum and maximum values were recorded and later used to constrain the model’s predictions within physical bounds.

The AE was trained on a dataset ranging from 1000 to 30000 instances over at least 2000 epochs. Early stopping was implemented to prevent overfitting by monitoring the validation loss and halting training once the loss stopped improving. The training utilized the ADAM optimizer [42], initialized with a learning rate of 10^{-3} . To adapt the learning rate dynamically, a `ReduceLROnPlateau` scheduler was applied [43], reducing the learning rate when the validation loss plateaued over several epochs. This helped the model avoid local minima and ensured smoother convergence.

Moreover, to prevent gradient explosions, gradient clipping was applied with a maximum norm of 1, ensuring stability during the backpropagation process. Weights for the model were initialized using the Xavier uniform initialization method [44], which promotes efficient learning by setting initial weights within a range that suits the network’s activation functions.

The training was conducted on NVIDIA GPUs, specifically Tesla V100 and A100, allowing for efficient computation and faster convergence. Depending on the configuration, e.g. the number of data instances in the training dataset, each training took approximately from 0.25 to 5 hours to complete, depending on the network size and on the batch size; see next sections for details.

3.4.1. Performance We evaluated the performance of our NN implementation during both the training and testing phases, with and without the inclusion of the terms \mathcal{L}_C , \mathcal{L}_{AC} and \mathcal{L}_b as defined in Eq. 16. The inclusion of these terms greatly improved the precision in reconstructing key physical quantities, such as mass, radius and tidal

deformability, when provided with any EoS input parameters. The total training time over a dataset of 5000 samples takes from ~ 20 min to ~ 5 hours, with the patience parameter set to values varying from 300 to 400, a batch size from 8 to 64 (which mostly influence the training time), and $n \in [16, 128]$ as specified in Table 1. Surprisingly, in terms of performance, the optimal number of dataset training instances ranges from 3000 to 5000. Increasing the number of samples beyond this range, even with adjustments to n and other network parameters, leads to a decrease in the network’s precision. We hypothesize that a relatively smaller number of samples may enhance the model’s generalization capability, preventing it from overfitting to the training data (see [45]).

4. Results

Every plot and result have been obtained using the following parameters: 5000 dataset training instances; `batch_size=4`; $n = 16$, patience of the scheduler $p = 50$; $[\alpha, \beta, \delta] = [100, 1, 0.1]$ (Eq. 16); dropout rate 0 (encoder) and 0.05 (decoder).

4.1. MRA Estimation from EoS: encoder

For several sets of EoS input parameters, the model demonstrates excellent agreement between the reconstructed and actual M - R and Λ - C relations. This strong performance highlights the model’s ability to accurately capture the physical relationships underlying NS properties.

Figure 3 presents an example encoder’s prediction for the TOV solutions of one of the generalized relativistic mean field EoS models, the DD2 EoS [46]. Interestingly, the network also exhibits a notable capacity for generalization, likely attributable to the incorporation of physics enforcing loss terms. By leveraging these constraints, the model is able to mitigate the impact of numerical errors of the TOV solutions present in the dataset itself, as presented in the lower panel of Fig. 3. The results discussed here are independent of the functional dropout, which is only active during the inference phase for EoS estimation, as will be described in the next subsection. The reasons behind this choice are explained in subsection 3.3.1.

This result suggests that the physics-informed loss acts as a form of regularization, allowing the network to maintain high precision and robustness in its predictions despite imperfections in the training data. Such a capability underscores the advantage of integrating domain-specific knowledge into the architecture, as it enables the model to overcome limitations that would otherwise hinder its accuracy and reliability.

In Fig. 4, we present a comparison of encoder’s performance with and without the physical constraints in the loss, using the WFF1 EoS from [47]. Note that the WFF1 EoS has proven to be challenging to reproduce. For this reason, it was specifically chosen to highlight the impact of the physics-informed loss. This difficulty can be attributed to the relatively stiff nature (i.e., steep $p(\rho)$ relation) of the EoS at low densities. While the current network demonstrates reasonable performance in reconstructing WFF1 EoS

Explainable autoencoder for neutron star dense matter parameter estimation

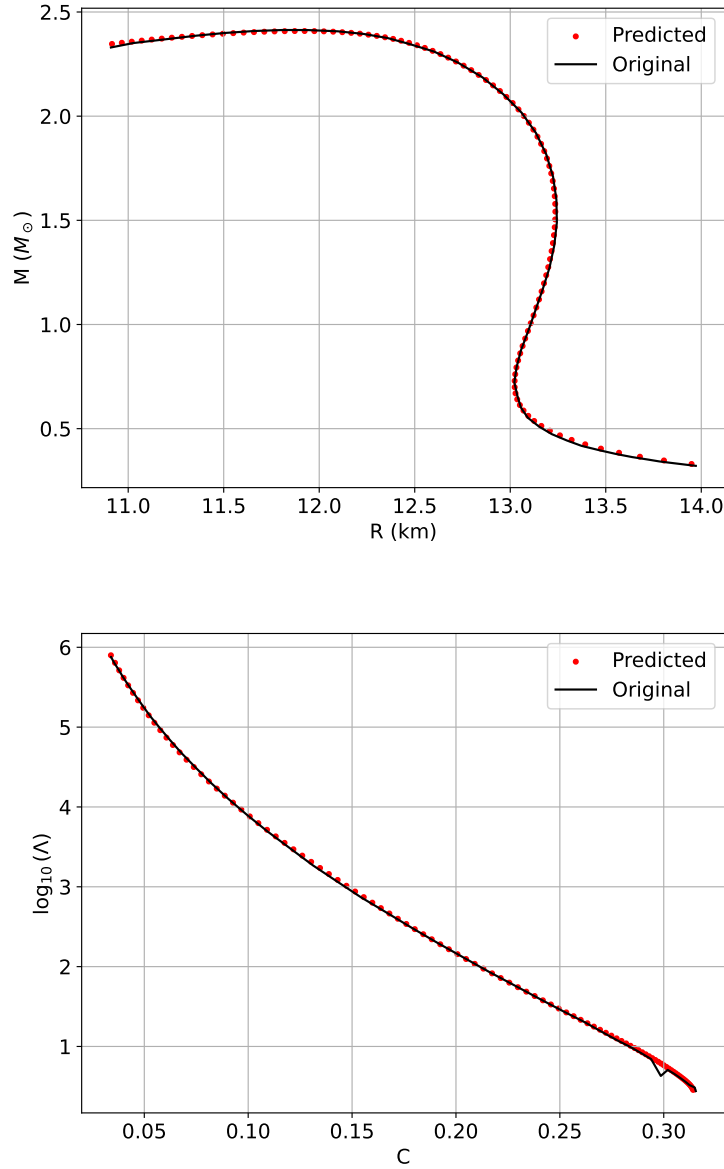


Figure 3. $M(R)$ diagram and Λ -compactness (Λ - C) relation for the DD2 EoS, generated using a network configured with $n = 16$, a batch size of 4, and a dropout rate of 0.05. Red dots represent the network’s predictions, while the black solid line corresponds to the numerical solutions of the analytical equations. It is evident that the network demonstrates an ability to generalize, e.g. in regions where TOV numerical errors are present in the tidal deformability calculations, see the point at $C \sim 0.3$ in the lower panel.

Explainable autoencoder for neutron star dense matter parameter estimation

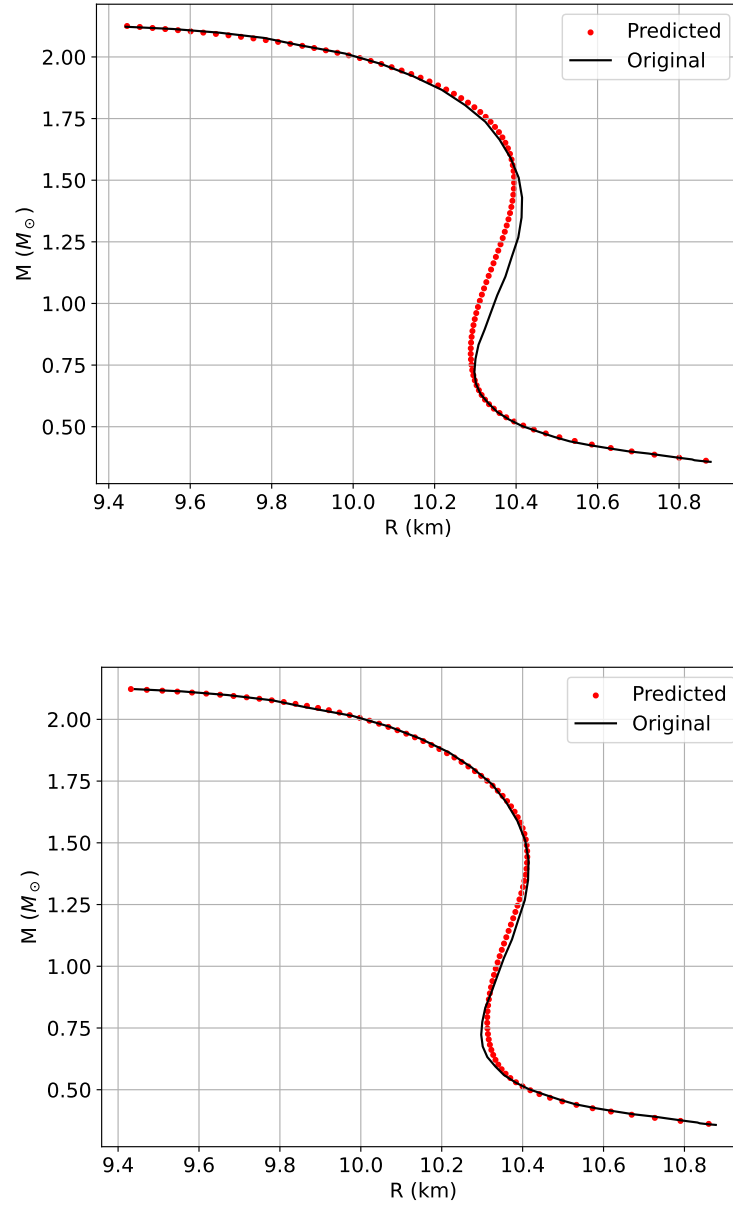


Figure 4. Top panel: the $M(R)$ diagram for the WFF1 EoS reproduced by a network with $n = 16$, a batch size of 4, and a dropout value of 0.05, *without* incorporating physical constraints. Bottom panel: The same $M(R)$ diagram reconstructed *with* the inclusion of physical constraints. The inclusion of physical constraints leads to a noticeably better agreement for intermediate masses between the predicted and expected results, demonstrating their impact on the network’s performance.

NS parameters, is far from being perfect and further improvements could be achieved through a more carefully constructed dataset. For instance, a dataset that includes a denser sampling of EoS parameter combinations in the low-density regime could help mitigate these challenges and enhance the network’s ability to generalize for such cases. In this case, the effect of incorporating physics-informed terms in the loss function becomes particularly evident, as shown in Fig. 4. Specifically, the radius predictions are significantly better constrained for intermediate masses when the physics-informed loss terms are included during training, resulting in more accurate and physically consistent reconstructions.

This improvement is not limited to the WFF1 EoS but is also observed for other EoSs, although in a less pronounced way. The presence of the physics-informed loss terms enhances the precision of the predictions in regions of high compactness, where tidal deformability exhibits steep gradients. These terms help the network focus on regions of the parameter space that are consistent with established physical principles, reducing the risk of erroneous predictions or “hallucinations” that could arise from interpolation in poorly constrained regions of the dataset. By grounding the learning process in physical relationships, the network is better equipped to avoid artifacts and produce reliable predictions, even in regions where the data is sparse. We underline that the NN model trained on piecewise polytropic EoS data allows us to approximate “realistic” EoS results with their piecewise polytropic versions by decoding their MR diagram together with $\Lambda(C)$.

4.2. EoS estimation from MRA: decoder

The decoder component of the network plays a central role in reconstructing the EoS from macroscopic NS observables. During this phase, the functional dropout is activated, enabling the model to estimate uncertainty by generating error bands in the predicted EoS profile. This uncertainty quantification is achieved through the Monte Carlo sampling, where the decoder is called multiple times with the same input data, creating a distribution of predictions. While the predictions are not always optimal for individual parameter combinations, the decoder statistically performs well across a wide range of scenarios. Specifically, it demonstrates the ability to predict the EoS for various combinations of input parameters p_1 , γ_1 , γ_2 , and γ_3 , capturing the underlying physical trends effectively. The network leverages the physics-informed constraints embedded in the training phase, allowing it to generalize well even when faced with noisy or imperfect input data.

The decoder is particularly valuable because it can also be applied to real observational data. As demonstrated in the next section, this capability allows the network to reconstruct the EoS directly from distribution of data, providing an efficient and reliable method for interpreting data from gravitational wave detections or other NS observations.

In Fig. 5, we present the reconstruction of the DD2 EoS as predicted by the network,

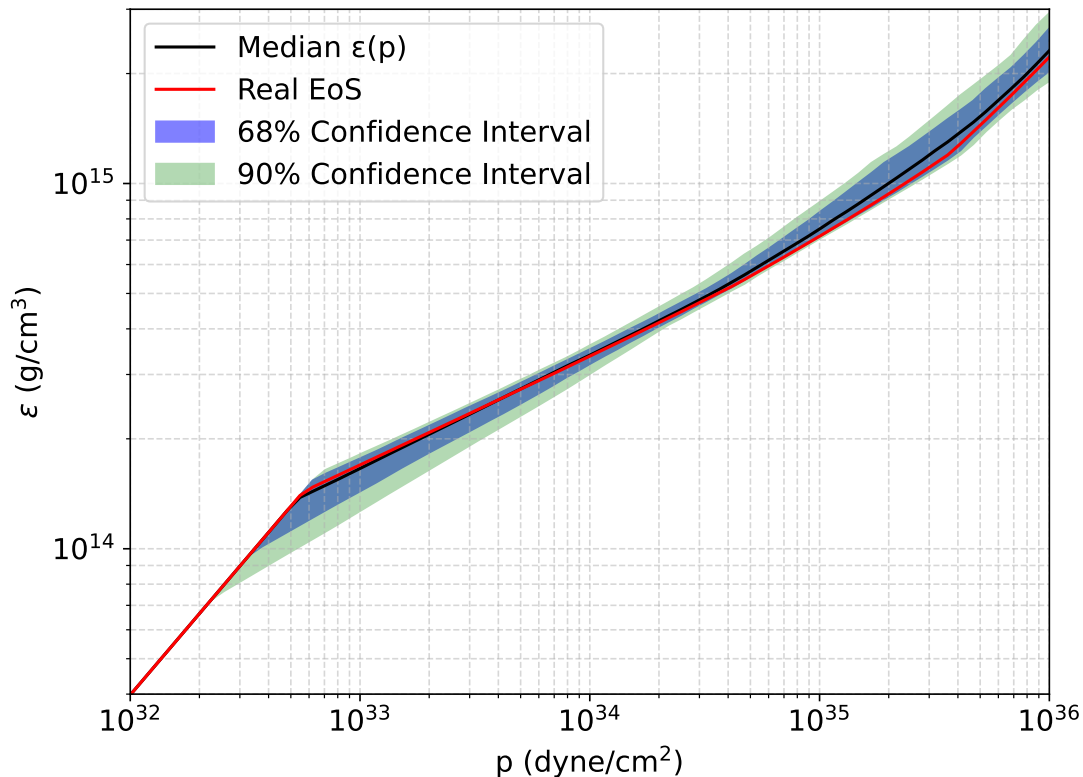


Figure 5. Model’s reconstruction of the DD2 EoS. The red line represents the true EoS, while the black line corresponds to the network’s median prediction of the mass-energy density $\epsilon(p)$. The shaded regions indicate the uncertainty in the predictions, with the blue region representing the 68% CI and the green region representing the 90% CI. The network accurately reproduces the true EoS over the entire range of pressures, with minor deviations in the high-density regime. These deviations remain within the uncertainty bounds, demonstrating the network’s ability to generalize and quantify its predictive uncertainty. The CIs reflect the effect of functional dropout during inference, enabling robust estimation even in regions where the training data may be sparse or numerical errors are present.

with estimated confidence intervals (CIs). The reconstruction demonstrates excellent agreement with the true EoS, with most regions falling well within the predicted error bands. However, the high-density regime poses a greater challenge for the network, as evidenced by slightly larger deviations. Even in this region, the predictions remain statistically consistent with the true EoS, highlighting the robustness of the approach despite the increased complexity of modeling very dense nuclear matter.

This difficulty in accurately predicting the high-density portion of the EoS arises from an intrinsic limitation previously discussed: the degeneracy in the mapping from macroscopic observables, such as mass and radius, to the underlying EoS parameters. Multiple combinations of p_1 , γ_1 , γ_2 , and γ_3 can yield similar mass-radius curves,

making it inherently challenging for the network to assign equal weight to all possible parameter combinations. While the network may not capture the degeneracy between EoS parameters with high precision in every individual prediction, it effectively accounts for this degeneracy in a statistical sense. E.g. in the case of WFF1, by introducing small perturbations (noise) to the input M , R , Λ data and using the decoder, the resulting EoS prediction align closer with the true EoS.

4.3. Application to a real case: GW170817 event

While the encoder component can be effectively used to solve the TOV equations and tidal deformability relations for piecewise polytropic EoSs, the decoder is particularly suited for application to real data. Its intrinsic capability of handling errors, given by the implementation of the Monte Carlo dropout, allows it to account for uncertainties in the input data, providing robust and reliable reconstructions even in the presence of error in input data themselves.

We utilize our best-trained decoder to infer the EoS from the gravitational-wave (GW) detection of a binary NS (BNS) inspiral GW170817 [48], which provided direct measurements of binary components' masses and tidal deformabilities, and indirect estimate of binary components' radii. The main properties of this event are presented in [49], while [50] provides constraints on the mass and radius of the two objects through the Bayesian inference on the GW signal.

We infer the EoS from GW170817 data by using the mass and radius posterior samples provided by [50] as inputs to the latent space of our decoder. The authors developed three distinct sets of mass M , radius R , and tidal deformability Λ posterior samples for both NSs, assuming one mass as strictly greater than the other and fixing the chirp mass at $\mathcal{M} = 1.186_{-0.001}^{+0.001} M_{\odot}$ [49]. The first set has been derived from samples of the antisymmetric tidal deformability, $\Lambda_a \equiv (\Lambda_2 - \Lambda_1)/2$, as defined in [51, 52], which is a function of the symmetric tidal deformability Λ_s and the mass ratio q . These samples were then used in the Λ - C relation to estimate the radii of the NSs. The second and third sets of posterior samples were instead generated integrating the TOV equation to determine the radius for each sample within a spectral parametrization of the EoS. The same EoS was assumed for both the NSs. For the third set only, a lower bound was applied to the maximum stable mass of a hypothetical NS, fixed at $1.97 M_{\odot}$. For this analysis, we use only the EoS insensitive posterior samples, to be absolutely agnostic in the comparison between our decoded EoS and the collaboration's Bayesian estimate. This M - R EoS insensitive dataset is shown in Fig. 7.

Notice that in this subsection, we are using 50% and 90% CIs, instead of 68% and 90%. We did this in order to make a direct comparison with the public Bayesian EoS estimates provided by the LIGO-Virgo collaboration (LVC) in [50]. Furthermore, we solve the TOV equations for each EoS CI limit, to verify its consistency with the data, as shown in Fig. 7.

We note that the LVC estimates of the EoS, which we compare to, are provided

only for the third set (under the assumption of a lower bound on the maximum mass of NSs). Nevertheless, our estimated EoS remains consistent with the LVC estimate, despite a noticeable discrepancy high-density end of the EoS (upper-right corner of Fig. 6). This behavior arises from two factors acting together. First of all, the EoS provided in [50] is based on a Bayesian inference method that incorporates an EoS prior, which includes a lower-bound constraint on the maximum mass of NSs. This assumption results in a stiffer EoS compared to the case without such a constraint. Secondly, the high-density region of the EoS is pure extrapolation, as the GW170817 event didn't provided information in this density range. Central pressures of the BNSs are estimated to be approximately $\sim 10^{35}$ dyn/cm², which coincides with the onset of the more significant discrepancy [50]. In this regime, the data are considerably less informative compared to the lower-density regions, further contributing to the observed (and expected) differences.

5. Conclusions

In this work, we presented a physics-informed AE capable of accurately reconstructing the dense matter EoS parameters for NSs while maintaining interpretability and physical consistency. The results achieved demonstrate both precision and robustness across a wide range of input parameters, even with a relatively small training dataset of just 5000 data instances.

One of the key findings of this study is the importance of incorporating physical constraints into the NN model. Without such constraints, the network loses its precision and often produces outputs that fall outside the physically meaningful range. In this case, the network would effectively function as a less accurate fitting machine, emphasizing the need for physics-informed approaches to enforce consistency and reliability in machine learning models applied to physical systems.

PIA serves as a proof-of-concept, providing a foundation for future improvements. For instance, further developments could focus on directly extracting features from gravitational waveforms, streamlining the data analysis process for NS observations. This capability will be particularly important as the upcoming Einstein Telescope and other next-generation observatories are expected to produce vast amounts of high-quality data. Fast, reliable, modular, and scalable tools like the proposed architecture will be essential to efficiently analyze these large datasets and extract meaningful physical insights.

The incorporation of even simple physical constraints, such as those based on compactness and tidal deformability, significantly improves the accuracy and reliability of the network. These constraints act as a form of regularization, allowing the network to produce physically consistent results even when trained on limited data. This makes PIA particularly robust for scientific applications where acquiring large, high-quality datasets can be challenging.

Another strength of this type of architecture lies in its modularity, which effectively

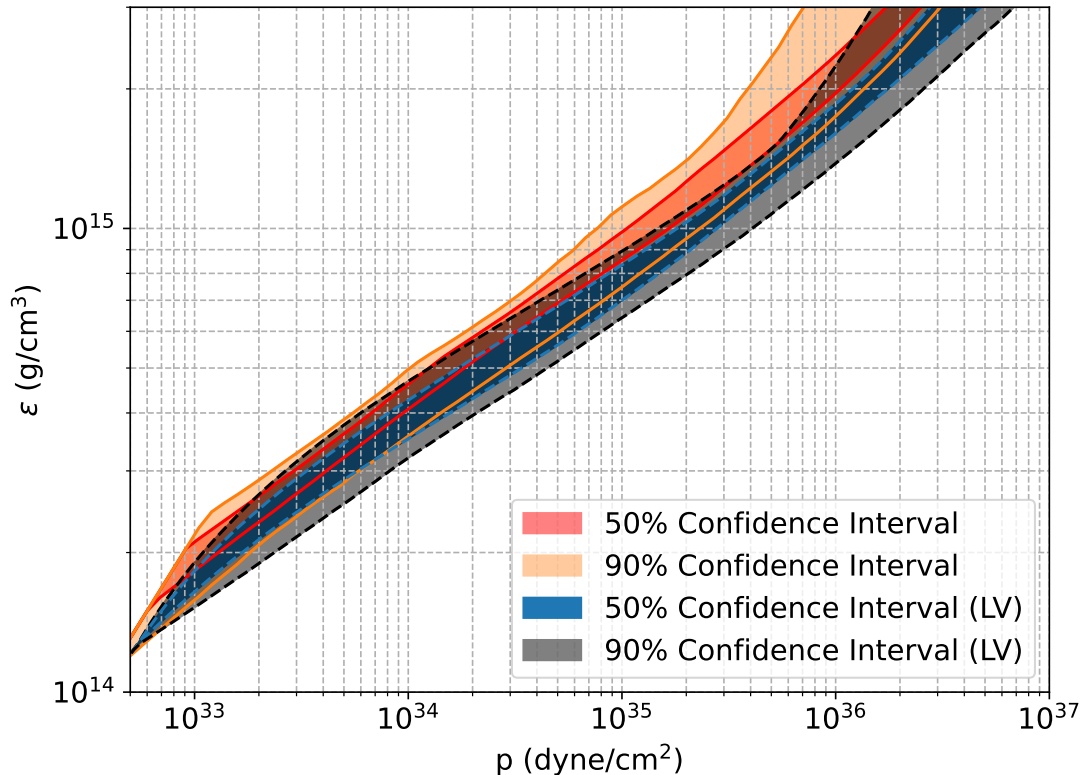


Figure 6. Comparison between our EoS estimation (red and orange confidence intervals) and the LIGO-Virgo collaboration’s EoS estimation (blue and gray confidence intervals). The shaded regions represent the 50% (red and blue) and 90% (orange and gray) confidence intervals for the energy density as a function of pressure. While both methods show strong agreement in the low and intermediate-density regimes, a notable discrepancy is observed at high densities. This discrepancy is likely due to the LVC incorporating constraints on the minimum maximum mass of NSs, a constraint that was not explicitly applied in our analysis. The results highlight the robustness of our method while emphasizing the influence of additional astrophysical constraints on the EoS predictions.

combines two networks in one. This modular design enhances the versatility of the framework, allowing it to be adapted and applied to a wide range of physical problems beyond neutron star modeling. The ability to treat the encoder and decoder as separate but interconnected components further increases the flexibility of the architecture.

While the network is functional and provides satisfactory results as it stands, it still requires fine-tuning of hyperparameters to achieve optimal performance for specific datasets or tasks. However, such fine-tuning is beyond the scope of this work. To encourage further development and exploration, the full code of PIA has been made publicly available on [github](#)[§].

[§] Both the training Python code and the testing Jupyter notebook, together with several trained

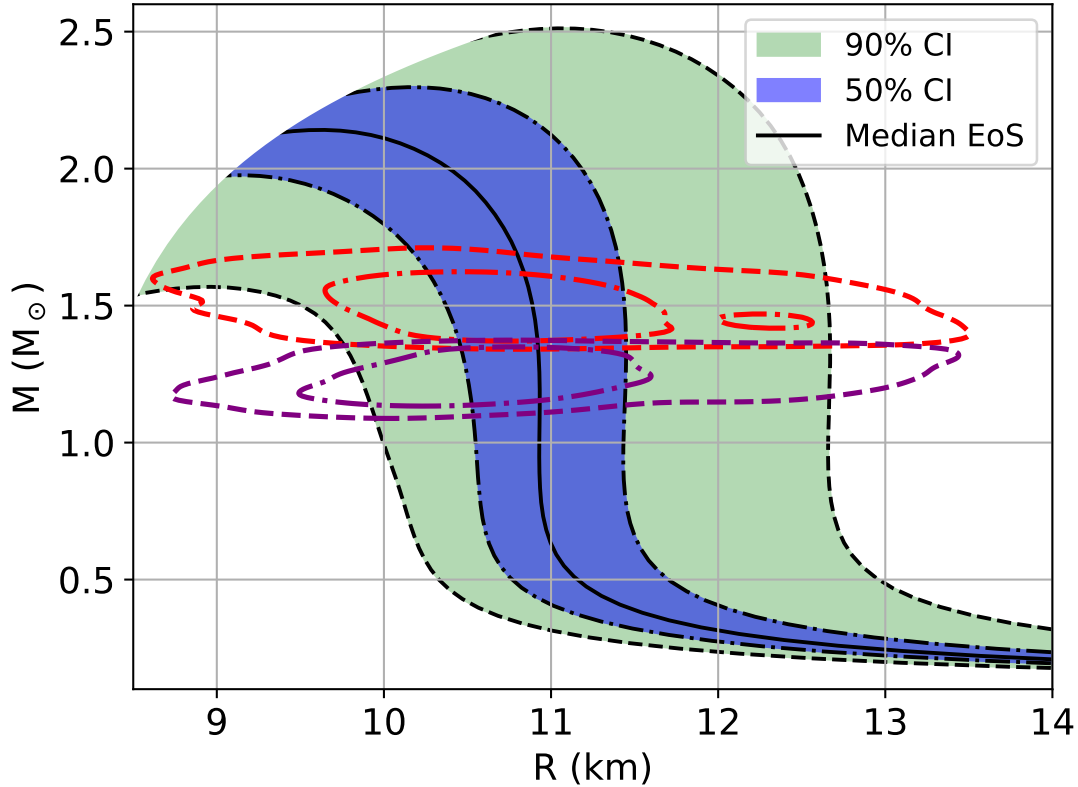


Figure 7. $M(R)$ diagram calculated from the CIs of the previously estimated EoS. The shaded regions represent the 50% (blue) and 90% (green) confidence intervals derived from the EoS estimation in Fig. 6. The solid black line corresponds to the median EoS prediction. The red and purple contours represent the MR constraints for GW170817 obtained by the LVC corresponding to 50% and 90% CIs. This plot aims to verify the consistency of the EoS predictions with the MR contours provided by the LVC analysis.

Finally, the current implementation of the network already allows for the estimation of the distribution of EoS parameters from macroscopic observables, such as mass, radius, and tidal deformability. This demonstrates its immediate applicability to NS studies and lays the groundwork for future enhancements in both accuracy and functionality.

For simplicity, in this work, we assumed that all NSs are described by a single EoS, implying the existence of only one family of compact stars. However, alternative scenarios, such as the two-families scenario [53, 54], where one EoS describes hadronic stars and another describes strange stars, are worth exploring. In this scenario, a hadronic star can transition into a strange star via specific microphysical mechanisms [55, 56], and the two families could potentially be distinguished through multimessenger observations [57–59].

Although we focus on the single-family EoS framework in this study, where the network predicts a single EoS, future developments could explore the possibility of probabilistically modeling two families of EoSs within the network. Such an approach would enable the simultaneous treatment of hadronic and strange star EoSs.

Acknowledgments

This research was partially supported by the Italian Ministry of Education, University and Research PRIN project no. 202275HT58 and the Polish National Science Center OPUS grant no. 2021/43/B/ST9/01714. We acknowledge using computing resources of the Nicolaus Copernicus Astronomical Center, Poland. Furthermore, we would like to thank Alessandro Drago for his valuable insights and constructive discussions.

Appendix A. Analysis of Auxiliary Loss in Physics-Informed Neural Networks

Appendix A.1. Combined Loss Functions

Generalizing the work in this paper, the total loss function combines a data-driven term $\mathcal{L}(\theta)$ with an auxiliary physics-informed loss $\mathcal{L}_{physics}(\theta)$:

$$\mathcal{L}_{total}(\theta) = \mathcal{L}(\theta) + \mathcal{L}_{physics}(\theta). \quad (\text{A.1})$$

Here, $\mathcal{L}(\theta)$ is the standard data-fitting loss (as in Eq. 3.1), while $\mathcal{L}_{physics}(\theta)$ is a physics-informed term enforcing known relationships between output components. For example,

$$\mathcal{L}_{physics}(\theta) = \text{MSE}(g(\hat{y}_i, \hat{y}_j, \dots), Y), \quad (\text{A.2})$$

where g is a known functional relationship between two or more of the predicted variables, and Y is either one of the predicted outputs itself or the ground truth.

By construction, if the target outputs \hat{y} (the ground truth) satisfy the known relationships encoded in $\mathcal{L}_{physics}(\theta)$, then the global minimizer of $\mathcal{L}(\theta)$ also minimizes $\mathcal{L}_{physics}(\theta)$. This ensures that adding $\mathcal{L}_{physics}(\theta)$ does not alter the global minimum, but may affect the optimization dynamics.

Appendix A.2. Effects on the global minimum

To analyze the effect of adding $\mathcal{L}_{physics}(\theta)$, we study the curvature around the global minimum θ^* .

Notice that the ground truth \hat{y}_i always satisfies the relationships encoded in $\mathcal{L}_{physics}(\theta)$. Therefore, $g(\hat{y}_i, \hat{y}_j, \dots) = \hat{Y}$. Supposing that the neural network perfectly fits the data at θ^* , then

$$y_{\theta^*}(x_i) = \hat{y}_i, \quad \forall i. \quad (\text{A.3})$$

Thus, at θ^* :

$$\mathcal{L}(\theta^*) = 0, \quad \mathcal{L}_{\text{physics}}(\theta^*) = 0, \quad \nabla \mathcal{L}(\theta^*) = 0, \quad \nabla \mathcal{L}_{\text{physics}}(\theta^*) = 0. \quad (\text{A.4})$$

Using a second-order Taylor expansion, the total loss near θ^* is:

$$\mathcal{L}_{\text{total}}(\theta) \approx \frac{1}{2} \Delta \theta^T H_{\mathcal{L}_{\text{total}}} \Delta \theta, \quad (\text{A.5})$$

where $\Delta \theta = \theta - \theta^*$ and $H_{\mathcal{L}_{\text{total}}}$ is the Hessian of $\mathcal{L}_{\text{total}}$ at θ^* . By linearity of differentiation:

$$H_{\mathcal{L}_{\text{total}}} = H_L + H_{\mathcal{L}_{\text{physics}}}, \quad (\text{A.6})$$

where H_L and $H_{\mathcal{L}_{\text{physics}}}$ are the Hessians of $\mathcal{L}(\theta)$ and $\mathcal{L}_{\text{physics}}(\theta)$, respectively.

The Hessian of a twice-differentiable function is the matrix of second derivatives. For two scalar functions $f(\theta)$ and $g(\theta)$, we have:

$$H_{f+g}(\theta) = H_f(\theta) + H_g(\theta). \quad (\text{A.7})$$

This result holds because differentiation is a linear operator. Therefore, the curvature of the combined loss $\mathcal{L}_{\text{total}}(\theta)$ is the sum of the curvatures of $\mathcal{L}(\theta)$ and $\mathcal{L}_{\text{physics}}(\theta)$. Since $\mathcal{L}(\theta)$ and $\mathcal{L}_{\text{physics}}(\theta)$ are sums of squared-error terms, their Hessians are positive semi-definite:

$$H_L \succeq 0, \quad H_{\mathcal{L}_{\text{physics}}} \succeq 0. \quad (\text{A.8})$$

For any direction $\Delta \theta$, the combined curvature satisfies:

$$\Delta \theta^T H_{\mathcal{L}_{\text{total}}} \Delta \theta = \Delta \theta^T H_L \Delta \theta + \Delta \theta^T H_{\mathcal{L}_{\text{physics}}} \Delta \theta \geq \Delta \theta^T H_L \Delta \theta. \quad (\text{A.9})$$

This shows that $\mathcal{L}_{\text{total}}(\theta)$ has at least as much curvature as $\mathcal{L}(\theta)$ in all directions, and generally more in directions where $H_{\mathcal{L}_{\text{physics}}}$ contributes positively. The increased curvature leads to a steeper gradient field near θ^* .

In conclusion, adding $\mathcal{L}_{\text{physics}}(\theta)$ improves the optimization on one hand by better defining the global minimum, reducing flat directions in parameter space around it, while on the other hand $\mathcal{L}_{\text{physics}}(\theta)$ acts as a regularizer by restricting the solution space to parameter regions that respect the physics-informed relationships.

References

- [1] D. E. Rumelhart, G. E. Hinton, and R. J. Williams. “Learning internal representations by error propagation”. In: *Parallel Distributed Processing: Explorations in the Microstructure of Cognition, Vol. 1: Foundations*. Cambridge, MA, USA: MIT Press, 1986, pp. 318–362.
- [2] Dor Bank, Noam Koenigstein, and Raja Giryes. “Autoencoders”. In: *arXiv e-prints*, arXiv:2003.05991 (Mar. 2020), arXiv:2003.05991. arXiv: [2003.05991](https://arxiv.org/abs/2003.05991) [[cs.LG](#)].

- [3] Shuangshuang Chen and Wei Guo. “Auto-Encoders in Deep Learning—A Review with New Perspectives”. In: *Mathematics* 11.8 (2023).
- [4] Umberto Michelucci. “An Introduction to Autoencoders”. In: *arXiv e-prints*, arXiv:2201.03898 (Jan. 2022), arXiv:2201.03898. arXiv: [2201.03898 \[cs.LG\]](#).
- [5] G. E. Hinton and R. R. Salakhutdinov. “Reducing the Dimensionality of Data with Neural Networks”. In: *Science* 313.5786 (2006), pp. 504–507. eprint: <https://www.science.org/doi/pdf/10.1126/science.1127647>.
- [6] Pengzhi Li, Yan Pei, and Jianqiang Li. “A comprehensive survey on design and application of autoencoder in deep learning”. In: *Applied Soft Computing* 138 (2023), p. 110176.
- [7] Luigi Scorzato. “Reliability and Interpretability in Science and Deep Learning”. In: *Minds and Machines* 34.3 (June 25, 2024), p. 27.
- [8] Aniek F. Markus, Jan A. Kors, and Peter R. Rijnbeek. “The role of explainability in creating trustworthy artificial intelligence for health care: A comprehensive survey of the terminology, design choices, and evaluation strategies”. In: *Journal of Biomedical Informatics* 113 (2021), p. 103655.
- [9] Alejandro Barredo Arrieta et al. “Explainable Artificial Intelligence (XAI): Concepts, taxonomies, opportunities and challenges toward responsible AI”. In: *Information Fusion* 58 (2020), pp. 82–115.
- [10] Richard C. Tolman. “Static Solutions of Einstein’s Field Equations for Spheres of Fluid”. In: *Physical Review* 55.4 (Feb. 1939), pp. 364–373.
- [11] J. R. Oppenheimer and G. M. Volkoff. “On Massive Neutron Cores”. In: *Physical Review* 55.4 (Feb. 1939), pp. 374–381.
- [12] Tanja Hinderer, Benjamin D. Lackey, Ryan N. Lang, and Jocelyn S. Read. “Tidal deformability of neutron stars with realistic equations of state and their gravitational wave signatures in binary inspiral”. In: *Phys. Rev. D* 81.12, 123016 (June 2010), p. 123016. arXiv: [0911.3535 \[astro-ph.HE\]](#).
- [13] Eric D. Van Oeveren and John L. Friedman. “Upper limit set by causality on the tidal deformability of a neutron star”. In: *Phys. Rev. D* 95.8, 083014 (Apr. 2017), p. 083014. arXiv: [1701.03797 \[gr-qc\]](#).
- [14] Kurt Hornik, Maxwell Stinchcombe, and Halbert White. “Multilayer feedforward networks are universal approximators”. In: *Neural Networks* 2.5 (1989), pp. 359–366.
- [15] G. Cybenko. “Approximation by superpositions of a sigmoidal function”. In: *Mathematics of Control, Signals, and Systems* 2.4 (Dec. 1989), pp. 303–314.
- [16] Márcio Ferreira and Constança Providência. “Unveiling the nuclear matter EoS from neutron star properties: a supervised machine learning approach”. In: *J. Cosmology Astropart. Phys.* 2021.7, 011 (July 2021), p. 011. arXiv: [1910.05554 \[nucl-th\]](#).

- [17] Yuki Fujimoto, Kenji Fukushima, and Koichi Murase. “Methodology study of machine learning for the neutron star equation of state”. In: *Phys. Rev. D* 98.2 (2018), p. 023019. arXiv: [1711.06748 \[nucl-th\]](#).
- [18] Yuki Fujimoto, Kenji Fukushima, and Koichi Murase. “Mapping neutron star data to the equation of state using the deep neural network”. In: *Phys. Rev. D* 101.5 (2020), p. 054016. arXiv: [1903.03400 \[nucl-th\]](#).
- [19] Yuki Fujimoto, Kenji Fukushima, and Koichi Murase. “Extensive studies of the neutron star equation of state from the deep learning inference with the observational data augmentation”. In: *Journal of High Energy Physics* 2021.3, 273 (Mar. 2021), p. 273. arXiv: [2101.08156 \[nucl-th\]](#).
- [20] Shriya Soma, Lingxiao Wang, Shuzhe Shi, Horst Stöcker, and Kai Zhou. “Neural network reconstruction of the dense matter equation of state from neutron star observables”. In: *J. Cosmology Astropart. Phys.* 2022.8, 071 (Aug. 2022), p. 071. arXiv: [2201.01756 \[hep-ph\]](#).
- [21] Filip Morawski and Michał Bejger. “Neural network reconstruction of the dense matter equation of state derived from the parameters of neutron stars”. In: *Astron. Astrophys.* 642 (2020), A78. arXiv: [2006.07194 \[astro-ph.HE\]](#).
- [22] Plamen G. Krastev. “Translating Neutron Star Observations to Nuclear Symmetry Energy via Deep Neural Networks”. In: *Galaxies* 10.1 (2022), p. 16. arXiv: [2112.04089 \[nucl-th\]](#).
- [23] Márcio Ferreira, Valéria Carvalho, and Constança Providência. “Extracting nuclear matter properties from the neutron star matter equation of state using deep neural networks”. In: *Phys. Rev. D* 106.10 (2022), p. 103023. arXiv: [2209.09085 \[nucl-th\]](#).
- [24] Plamen G. Krastev. “A Deep Learning Approach to Extracting Nuclear Matter Properties from Neutron Star Observations”. In: *Symmetry* 15.5 (2023), p. 1123. arXiv: [2303.17146 \[nucl-th\]](#).
- [25] Ming-Zhe Han, Jin-Liang Jiang, Shao-Peng Tang, and Yi-Zhong Fan. “Bayesian Nonparametric Inference of the Neutron Star Equation of State via a Neural Network”. In: *Astrophys. J.* 919.1 (2021), p. 11. arXiv: [2103.05408 \[hep-ph\]](#).
- [26] Shriya Soma, Lingxiao Wang, Shuzhe Shi, Horst Stöcker, and Kai Zhou. “Reconstructing the neutron star equation of state from observational data via automatic differentiation”. In: *Phys. Rev. D* 107.8 (2023), p. 083028. arXiv: [2209.08883 \[astro-ph.HE\]](#).
- [27] Filip Morawski and Michał Bejger. “Detecting dense-matter phase transition signatures in neutron star mass-radius measurements as data anomalies using normalizing flows”. In: *Phys. Rev. C* 106.6, 065802 (Dec. 2022), p. 065802. arXiv: [2212.05480 \[astro-ph.HE\]](#).

- [28] Ameya Thete, Kinjal Banerjee, and Tuhin Malik. “Realizing the potential of deep neural network for analyzing neutron star observables and dense matter equation of state”. In: *Phys. Rev. D* 108.6 (2023), p. 063028.
- [29] Valéria Carvalho, Márcio Ferreira, Constança Providência, and Michał Bejger. “Detecting the third family of compact stars with normalizing flows”. In: (Mar. 2024). arXiv: [2403.09398](https://arxiv.org/abs/2403.09398) [[nucl-th](#)].
- [30] Márcio Ferreira and Michał Bejger. “Conditional variational autoencoder inference of neutron star equation of state from astrophysical observations”. In: *Phys. Rev. D* 111 (2 Jan. 2025), p. 023035.
- [31] M. Raissi, P. Perdikaris, and G.E. Karniadakis. “Physics-informed neural networks: A deep learning framework for solving forward and inverse problems involving nonlinear partial differential equations”. In: *Journal of Computational Physics* 378 (2019), pp. 686–707.
- [32] Renato Giorgiani Nascimento, Kajetan Fricke, and Felipe Antonio Chegury Viana. “A tutorial on solving ordinary differential equations using Python and hybrid physics-informed neural network”. In: *Eng. Appl. Artif. Intell.* 96 (2020), p. 103996.
- [33] Maziar Raissi, Paris Perdikaris, Nazanin Ahmadi, and George Em Karniadakis. *Physics-Informed Neural Networks and Extensions*. 2024. arXiv: [2408.16806](https://arxiv.org/abs/2408.16806) [[cs.LG](#)].
- [34] P. B. Demorest, T. Pennucci, S. M. Ransom, M. S. E. Roberts, and J. W. T. Hessels. “A two-solar-mass neutron star measured using Shapiro delay”. In: *Nature* 467.7319 (Oct. 2010), pp. 1081–1083. arXiv: [1010.5788](https://arxiv.org/abs/1010.5788) [[astro-ph.HE](#)].
- [35] Jocelyn S. Read, Benjamin D. Lackey, Benjamin J. Owen, and John L. Friedman. “Constraints on a phenomenologically parametrized neutron-star equation of state”. In: *Physical Review D* 79.12 (June 2009).
- [36] F. Douchin and P. Haensel. “A unified equation of state of dense matter and neutron star structure”. In: *A&A* 380 (Dec. 2001), pp. 151–167. arXiv: [astro-ph/0111092](https://arxiv.org/abs/astro-ph/0111092) [[astro-ph](#)].
- [37] Nikolaos Stergioulas. *Tolman-Oppenheimer-Volkoff solutions with piecewise polytropic EOS*. <https://github.com/niksterg/pyTOVpp>. 2019.
- [38] Feryal Özel and Paulo Freire. “Masses, Radii, and the Equation of State of Neutron Stars”. In: *Annual Review of Astronomy and Astrophysics* 54.1 (Sept. 2016), pp. 401–440.
- [39] Swarnim Shashank, Fatemeh Hossein Nouri, and Anshu Gupta. “f-mode oscillations of compact stars with realistic equations of state in dynamical spacetime”. In: *New Astronomy* 104 (2023), p. 102067.
- [40] Carolyn A. Raithel and Elias R. Most. “Tidal deformability doppelgänger: Implications of a low-density phase transition in the neutron star equation of state”. In: *Physical Review D* 108.2 (July 2023).

- [41] Yarin Gal and Zoubin Ghahramani. “Dropout as a bayesian approximation: Representing model uncertainty in deep learning”. In: *international conference on machine learning*. PMLR. 2016, pp. 1050–1059.
- [42] Diederik P. Kingma and Jimmy Ba. *Adam: A Method for Stochastic Optimization*. 2017. arXiv: [1412.6980](https://arxiv.org/abs/1412.6980) [cs.LG].
- [43] *ReduceLRonPlateau pytorch v2.5 documentation*. https://pytorch.org/docs/stable/generated/torch.optim.lr_scheduler.ReduceLRonPlateau.html. Accessed: 2025-01-22.
- [44] Xavier Glorot and Yoshua Bengio. “Understanding the difficulty of training deep feedforward neural networks”. In: *International Conference on Artificial Intelligence and Statistics*. 2010.
- [45] Matthew Olson, Abraham Wyner, and Richard Berk. “Modern Neural Networks Generalize on Small Data Sets”. In: *Advances in Neural Information Processing Systems*. Ed. by S. Bengio et al. Vol. 31. Curran Associates, Inc., 2018.
- [46] S. Typel, G. Röpke, T. Klähn, D. Blaschke, and H. H. Wolter. “Composition and thermodynamics of nuclear matter with light clusters”. In: *Phys. Rev. C* 81.1, 015803 (Jan. 2010), p. 015803. arXiv: [0908.2344](https://arxiv.org/abs/0908.2344) [nucl-th].
- [47] R. B. Wiringa, V. Fiks, and A. Fabrocini. “Equation of state for dense nucleon matter”. In: *Phys. Rev. C* 38 (2 Aug. 1988), pp. 1010–1037.
- [48] B. P. Abbott et al. “GW170817: Observation of Gravitational Waves from a Binary Neutron Star Inspiral”. In: *Physical Review Letters* 119.16 (Oct. 2017).
- [49] B. P. Abbott et al. “Properties of the Binary Neutron Star Merger GW170817”. In: *Phys. Rev. X* 9 (1 Jan. 2019), p. 011001.
- [50] B. P. Abbott et al. “GW170817: Measurements of Neutron Star Radii and Equation of State”. In: *Phys. Rev. Lett.* 121 (16 Oct. 2018), p. 161101.
- [51] Kent Yagi and Nicolás Yunes. “Binary Love relations”. In: *Classical and Quantum Gravity* 33.13 (June 2016), 13LT01.
- [52] Katerina Chatziioannou, Carl-Johan Haster, and Aaron Zimmerman. “Measuring the neutron star tidal deformability with equation-of-state-independent relations and gravitational waves”. In: *Physical Review D* 97.10 (May 2018).
- [53] Alessandro Drago, Andrea Lavagno, Giuseppe Pagliara, and Daniele Pigato. “The scenario of two families of compact stars: 1. Equations of state, mass-radius relations and binary systems”. In: *Eur. Phys. J. A* 52.2 (2016), p. 40. arXiv: [1509.02131](https://arxiv.org/abs/1509.02131) [astro-ph.SR].
- [54] I. Bombaci, A. Drago, D. Logoteta, G. Pagliara, and I. Vidaña. “Was GW190814 a Black Hole–Strange Quark Star System?” In: *Phys. Rev. Lett.* 126.16 (2021), p. 162702. arXiv: [2010.01509](https://arxiv.org/abs/2010.01509) [nucl-th].
- [55] Alessandro Drago and Giuseppe Pagliara. “Why can hadronic stars convert into strange quark stars with larger radii”. In: *Phys. Rev. D* 102.6 (2020), p. 063003. arXiv: [2007.03436](https://arxiv.org/abs/2007.03436) [nucl-th].

- [56] Mirco Guerrini, Giuseppe Pagliara, Alessandro Drago, and Andrea Lavagno. “Thermal Fluctuations of Matter Composition and Quark Nucleation in Compact Stars”. In: *Astrophys. J.* 974.1 (2024), p. 45. arXiv: [2404.06463 \[nucl-th\]](#).
- [57] Francesco Di Clemente, Alessandro Drago, and Giuseppe Pagliara. “Is the Compact Object Associated with HESS J1731-347 a Strange Quark Star? A Possible Astrophysical Scenario for Its Formation”. In: *Astrophys. J.* 967.2 (2024), p. 159. arXiv: [2211.07485 \[astro-ph.HE\]](#).
- [58] Francesco Di Clemente, Alessandro Drago, and Giuseppe Pagliara. “Merger of a Neutron Star with a Black Hole: One-family versus Two-families Scenario”. In: *Astrophys. J.* 929.1 (2022), p. 44. arXiv: [2106.16151 \[astro-ph.HE\]](#).
- [59] Lowri Wyn Prys Mathias, Francesco Di Clemente, Mattia Bulla, and Alessandro Drago. “Black hole–neutron star mergers: using kilonovae to constrain the equation of state”. In: *Mon. Not. Roy. Astron. Soc.* 527.4 (2023), pp. 11053–11065. arXiv: [2309.00890 \[astro-ph.HE\]](#).